

Electronic, spin-state, and magnetic transitions in $\text{Ba}_2\text{Co}_9\text{O}_{14}$ investigated by x-ray spectroscopies and neutron diffraction

J. Herrero-Martín,^{1,*} J. Padilla-Pantoja,² S. Lafuerza,³ A. Romaguera,² F. Fauth,¹ J. S. Reparaz,² and J. L. García-Muñoz^{2,†}

¹ALBA Synchrotron Light Facility, 08290 Cerdanyola del Vallès, Barcelona, Spain

²Institut de Ciència de Materials de Barcelona, ICMAB-CSIC, Campus Universitari de Bellaterra, E-08193 Bellaterra, Spain

³ESRF-The European Synchrotron, 71 Avenue des Martyrs, Grenoble, France

(Received 24 February 2017; published 15 June 2017)

The mixed $\text{Ba}_2\text{Co}_9\text{O}_{14}$ $\text{Co}^{2+}/\text{Co}^{3+}$ system undergoes an insulator-insulator transition at $T_{\text{SS}} \sim 567$ K that arises from a spin-state transition at trivalent cobalt sites. Below this temperature, Co1, Co2, and Co4 are nonmagnetic ($S = 0$, low spin). Ferromagnetically aligned Co5 spins are sandwiched between antiparallel planes of Co3 spins below $T_N \approx 41$ K. The successive antiferromagnetic trilayers are inverted along the c axis (compatible with C_c2/c , C_c2/m , or P_S-1 magnetic space groups, depending on the moment orientation in the ab plane). The origin of the resistivity drop on warming was investigated by means of neutron and x-ray diffraction, x-ray absorption and emission spectroscopies, and x-ray magnetic circular dichroism. Charge-transfer multiplet calculations confirm that the divalent Co sites are both in an $S = 3/2$ high spin state. Independently, the analysis of measured Co $K\beta$ x-ray emission spectroscopy spectra agrees with this model. The magnetic moment from divalent Co5 ions is not fully ordered, likely due to the competition between magnetic anisotropy and weak supersuperexchange interactions, but not to covalency effects. Results agree with the spin blockade of electronic transport being partially removed at the octahedral trimers and also at the Co_4O_6 units within the CdI_2 -type layer.

DOI: [10.1103/PhysRevB.95.235129](https://doi.org/10.1103/PhysRevB.95.235129)

I. INTRODUCTION

The spin-state (SS) of trivalent cobalt is being examined in a variety of cobalt oxides due to its proven ability to condition their electric transport, magnetic, and electronic properties [1–7]. The presence of metal-insulator transitions (MITs) in cobalt oxides can be an indication and allows investigating spin-state changes phenomena. They are found in a wide variety of compounds with perovskite and related structures such as LnCoO_3 [1–3], $\text{Ln}_{1-x}\text{A}_x\text{CoO}_3$ [4–7], the layered double perovskites $\text{LnBaCo}_2\text{O}_{5.50}$ [8,9], or more complex structures [10].

One of the most recently synthesized cobaltites is $\text{Ba}_2\text{Co}_9\text{O}_{14}$ (BCO), a charge-ordered $\text{Co}^{2+}/\text{Co}^{3+}$ rhombohedral $R-3m$ system. It was isolated by J. Sun *et al.* [10] and Ehora *et al.* [11], who identified new building blocks (called T') in its structure, by analogy with the T blocks of the barium hexaferrites. The $\text{Ba}_{n+1}\text{Co}_n\text{O}_{3n+3}(\text{Co}_8\text{O}_8)$ family of intergrowth BCO compounds attracted initially the interest as potential candidates for thermoelectric materials, and as cathodes for solid oxide fuel cells [10–12]. As the $n = 1$ member of this series, BCO is thermally stable up to 1000 °C where it decomposes into CoO and BaCoO_{3-d} . Its structure can be described as an intergrowth of CdI_2 -type $\text{CoO}_{6/3}$ layers and Co_3O_{12} octahedral trimers that are connected by corner-sharing CoO_4 tetrahedra [10,11]. Trimers act as vertical bridges connecting successive $\text{CoO}_{6/3}$ layers along- c . The hexagonal cell is formed by three T' blocks, each one occupying the space between two successive CdI_2 -type layers. The catalytic activity of BCO has been explored by Li *et al.* [12] for the $\text{Co}^{2+}/\text{Co}^{3+}$ couple.

The BCO crystal unit cell contains five crystallographically independent Co sites (Co_i), with octahedral (Co_i ,

$i = 1, 2, 4, 5$) and tetrahedral (Co_3) local coordination [10,11]. The Co_2 octahedron shares its opposite triangular faces with two Co_1 octahedra, forming the Co_3O_{12} octahedral trimer; the Co_4 and the Co_5 octahedra share edges to form the CdI_2 -type $\text{CoO}_{6/3}$ layers; and the Co_3 tetrahedron shares corners with both the Co_3O_{12} trimers and the CdI_2 -type $\text{CoO}_{6/3}$ layers.

The Curie-Weiss susceptibility below room temperature was found to be compatible with low spin Co^{3+} ($S = 0$) at trivalent sites (Co_1 , Co_2 , Co_4) [11,13] and low-temperature neutron diffraction revealed long-range antiferromagnetic (AFM) order below 41 K. Co_3 and Co_5 cobalt positions were proposed by Ehora *et al.* to be occupied by divalent Co ions in a high spin state (HS, $S = 3/2$) [11]. Using neutron data, they also proposed an AFM stacking of the magnetic layers along c , with different magnetic moments in the ab plane at the octahedral and tetrahedral sites. Interestingly, they noticed that the magnetic coupling between tetrahedral and octahedral divalent Co sites must take place through $\text{Co}^{2+} - \text{O} - \text{O} - \text{Co}^{2+}$ supersuperexchange (SSE) paths exclusively. In apparent contradiction with the assumption of HS Co^{2+} ions at Co_3 and Co_5 positions, based on neutron data of limited quality that presented several impurity peaks, the ordered moment derived for the last position was much smaller than expected for the $S = 3/2$, $t_{2g}^5 e_g^2$ configuration.

Likewise, some discrepancies are found in the electronic conductivity reported by different groups. Two separate anomalies appear in the resistivity curve of Ref. [11], whereas a single conductivity transition near 600 K was confirmed later by other authors [12,13]. Although a noticeable increase of the conductivity around 570 K was initially attributed to the formation of oxygen vacancies [11], the changes in the 500–600-K range were later identified as a possible spin-state transition (T_{SS}) by J.-G. Cheng *et al.* [13] on the basis of synchrotron x-ray diffraction (XRD) and x-ray-absorption spectroscopy (XAS) measurements. The evolution of the O K XAS spectra of BCO as a function of temperature was

*jherrero@cells.es

†garcia.munoz@icmab.es

attributed to the occupation of higher spin states on Co1 and Co2 sites on warming. This conclusion resulted from the observation of certain anomalies in the XRD patterns, which—within the experimental accuracy—were not observed on Co4 sites. On the other hand, a neutron-diffraction study of this complex structure at high temperatures (above 300 K) thereby comprehending the aforementioned conductivity transition has been missing to date.

In this paper we report a full accounting of the possible low-temperature magnetic phases and the magnetic space groups, and of the high-temperature structural and spin-state evolution displayed by $\text{Ba}_2\text{Co}_9\text{O}_{14}$ up to 800 K. The investigation of the full magnetic symmetry and the structural distortions across T_{SS} provides a coherent insight in the cause of the sudden electrical conductivity changes around 567 K. Soft x-ray-absorption, x-ray magnetic circular dichroism, and $K\beta$ x-ray emission spectroscopies have been applied to probe the electronic and spin state of Co ions at the different crystallographic sites, paying particular attention to the differences between the two Co^{2+} sites (Co3, Co5) in

the structure. Despite a strong ordered moment reduction at divalent Co5 sites, a high spin configuration for all Co^{2+} ions (Co3, Co5) in the structure appears to be the only solution matching Co $L_{2,3}$ x-ray-absorption spectra.

II. EXPERIMENTAL DETAILS

Polycrystalline ceramic samples of $\text{Ba}_2\text{Co}_9\text{O}_{14}$ were prepared by the conventional solid-state reaction method, as reported in Ref. [11]. High-purity Co_3O_4 and BaCO_3 were used as precursors. After regrinding of the resulting pellets, the compression and the annealing processes were repeated several times at temperatures ranging between 850 and 890 °C. After the last annealing the samples were slowly cooled down to room temperature (RT) at a rate of 120 °C/h in air. The samples’ quality was checked by x-ray-diffraction patterns collected at RT using a Siemens D-5000 diffractometer and $\text{Cu-K}\alpha$ radiation. They were single phase and free from impurities. Rietveld refinements showed that the obtained BCO powders presented a certain degree of preferred orientation (needlelike).

The magnetic response to dc and ac magnetic fields was measured using a superconducting quantum interferometer device (SQUID) and a physical properties measuring system (PPMS) from Quantum Design. ac magnetization was measured at frequency values of $\gamma = 1.1, 3.3,$ and 9.9 kHz, and with an amplitude of 10 Oe. For the electrical transport measurements of BCO pellets, metallic silver (Ag) electrodes

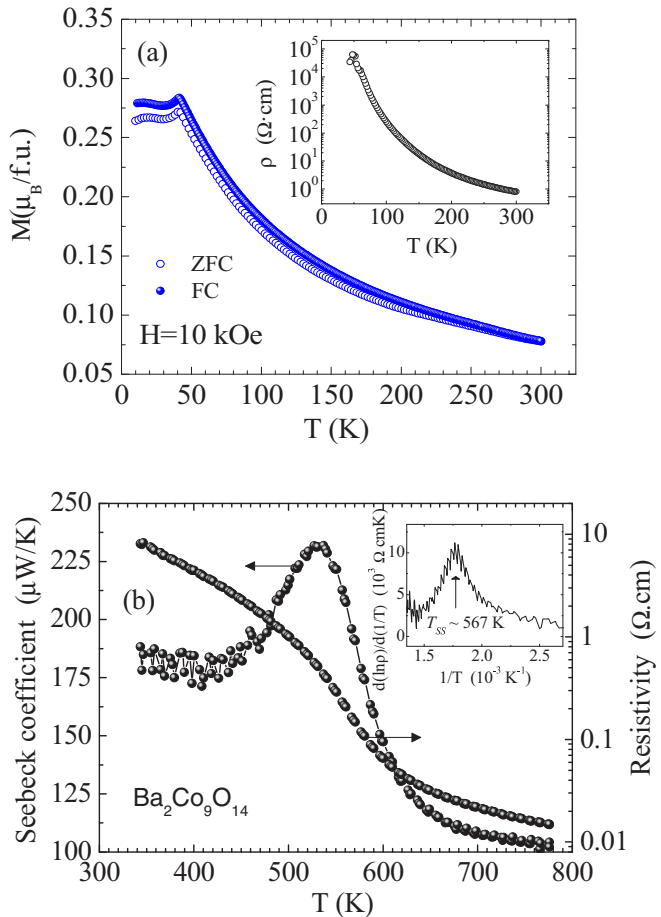


FIG. 1. (a) Temperature dependence of magnetization of $\text{Ba}_2\text{Co}_9\text{O}_{14}$ measured at 10 kOe using the direct current (dc). Open and solid circles refer to measurement under the zero-field-cooling (ZFC) and field-cooling (FC) conditions, respectively. The inset shows the resistivity curve. (b) Temperature dependence of the Seebeck coefficient (left axis) and the resistivity (right axis) at high temperature. The inset shows the $d[(\ln\rho)]/d(1/T)$ vs $1/T$ curve with a maximum at $T_{SS} = 567$ K.

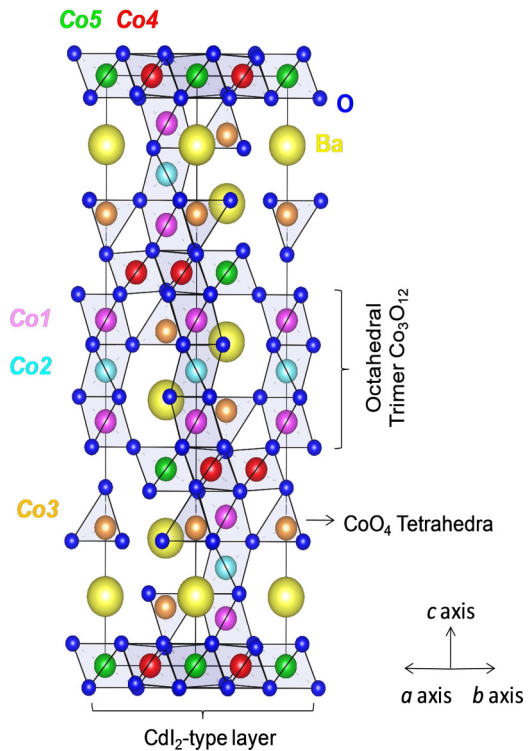


FIG. 2. Crystallographic projection of $\text{Ba}_2\text{Co}_9\text{CoO}_{14}$. The five crystallographically independent Co sites are shown with different colors in the structure (Co1, pink balls; Co2 light blue balls; Co3 orange balls; Co4 red balls, and Co5 green balls). Ba and O atoms are represented in yellow and dark blue, respectively.

TABLE I. Structural parameters of $\text{Ba}_2\text{Co}_9\text{O}_{14}$ refined at four representative temperatures up to 800 K using high-resolution NPD data and the $R\text{-}3m$ (166) symmetry (hexagonal cell).

$T(\text{K})$	300 K	420 K	600 K	800 K
a (Å)	5.6921(7)	5.7003(4)	5.7277(4)	5.7516(4)
b (Å)	5.6921(7)	5.7003(4)	5.7277(4)	5.7516(4)
c (Å)	28.8936(4)	28.9577(4)	29.2459(4)	29.4996(5)
γ (deg)	120	120	120	120
Atom coordinates:	Ba $6c(0, 0, z)$, Co1 $6c(0, 0, z)$, Co2 $3b(0, 0, 1/2)$, Co3 $6c(0, 0, z)$, Co4 $9e(1/2, 0, 0)$, Co5 $3a(0, 0, 0)$, O1 $18h(x, -x, z)$, O2 $6c(0, 0, z)$, O3 $18h(x, -x, z)$			
Ba (z)	0.8835(8)	0.8835(2)	0.8848(2)	0.8825(3)
Ba, B_{iso} (Å ²)	0.30(8)	0.40(9)	1.12(1)	1.54(2)
Co1 (z)	0.5884(4)	0.5884(5)	0.5881(5)	0.5870(6)
Co1, B_{iso} (Å ²)	0.21(3)	0.41(5)	0.74(6)	1.05(6)
Co2, B_{iso} (Å ²)	0.21(3)	0.41(5)	0.74(6)	1.05(6)
Co3 (z)	0.2330(2)	0.2330(3)	0.2361(4)	0.2349(5)
Co3, B_{iso} (Å ²)	0.21(3)	0.41(5)	0.74(6)	1.05(6)
Co4, B_{iso} (Å ²)	0.21(3)	0.41(5)	0.74(6)	1.05(6)
Co5, B_{iso} (Å ²)	0.21(3)	0.41(5)	0.74(6)	1.05(6)
O1 (x)	0.1506(7)	0.1512(6)	0.1542(9)	0.1565(2)
O1 (z)	0.4563(7)	0.4560(8)	0.4547(1)	0.4547(1)
O1, B_{iso} (Å ²)	0.31(4)	0.45(4)	0.94(5)	1.46(7)
O2 (z)	0.6996(6)	0.6996(1)	0.6993(2)	0.6994(2)
O2, B_{iso} (Å ²)	0.60(7)	0.75(8)	0.86(1)	0.817(2)
O3 (x)	0.4851(6)	0.4852(6)	0.4874(8)	0.4907(1)
O3 (z)	0.2954(8)	0.2954(9)	0.2960(1)	0.2965(1)
O3, B_{iso} (Å ²)	0.41(1)	0.57(4)	0.75(5)	1.25(6)
Agreement parameters:				
χ^2 (%)	0.74	0.71	0.78	0.77
R_B (%)	3.80	4.19	5.20	6.62

(500 nm) were deposited on top of the surface using a mechanical mask. In order to obtain a better adhesion of the Ag on the BCO pellet a thermal annealing was conducted at 450 °C for 1 h under O_2 atmosphere. The contacts were done with platinum wiring (25 μm) and the dc resistivity was measured at temperatures ranging 10–300 K via the four-probe method using a PPMS. Additional Seebeck and electrical conductivity measurements were recorded at high temperatures using a commercial setup (Linseis LSR-3). For the thermoelectric measurements the samples were cut into square bars of approximately 1 cm length and with square cross section. A temperature gradient of 50 K was applied across the sample, and the Seebeck coefficient was measured using two Alumel thermocouples close to the middle of the samples where the temperature gradient was about 10 K. The measurements were calibrated using Constantan, a cooper-nickel alloy calibration standard.

Neutron-diffraction experiments were carried out at the high-flux reactor of the Institut Laue Langevin (Grenoble, France) using the high-intensity D1B and high-angular resolution D2B diffractometers. The crystal structure evolution across the high-temperature transition was studied using the high-intensity mode of D2B and $\lambda = 1.594$ Å, warming up the sample in a furnace from RT to 800 K. Below RT, the Co spins behavior in the five distinct Wyckoff positions occupied by cobalt ions was investigated on the D1B diffractometer using an Orange cryostat and a neutron wavelength $\lambda = 2.52$ Å.

The detector of D1B covers an angular range of 128° and its 1280 gold wires provide an angular definition of 0.1° between neutron detection points. Additionally, synchrotron x-ray powder-diffraction patterns (SXRPD) were collected at the BL04-MSPD beamline [14] of the ALBA Synchrotron Light Facility (Barcelona, Spain) using $\lambda = 0.4128$ Å. Patterns were recorded every 80 s by the Mythen banana-type detector while warming the sample from 300 up to 773 K at a rate of 4 K/min. The working temperature was set using a CYBERSTAR hot air blower. Structural and magnetic Rietveld refinements were made using the FULLPROF program [15]. Crystallographic tools from the Bilbao Crystallographic server [16–18] and ISOTROPY Software Suite [19] were also used.

Soft x-ray-absorption spectroscopy (XAS) and x-ray magnetic circular dichroism (XMCD) measurements at the Co $L_{2,3}$ edges were performed at the BL29-BOREAS beamline of the ALBA Synchrotron [20]. Data were recorded in Total Electron Yield (TEY) mode, the samples having been scraped *in situ* under ultrahigh vacuum ($\sim 10^{-9}$ mbar) conditions prior to collecting spectra. CoO was simultaneously measured as an energy calibration reference. The XMCD spectra were recorded using alternatively left and right circularly polarized x rays produced by an APPLE II undulator and a superconducting split coil setup generating a magnetic field up to 6 T in the direction of propagation of the incident photons. The photon flux was about 5×10^{11} photons/s with an energy resolution of ~ 100 meV.

$K\beta$ x-ray emission spectroscopy (XES) measurements were carried out at the ID26 beamline of the European Synchrotron Radiation Facility (Grenoble, France). The incident photon energy was tuned at 7800 eV by means of a pair of cryogenically cooled Si (311) monochromator crystals. The emitted x rays were analyzed using a set of four spherically bent Ge (444) crystals that were arranged with the sample and photon detector in a vertical Rowland geometry ($R = 1$ m) at 90° horizontal scattering angle. The overall energy resolution was about 400 meV. All emission spectra were normalized by their area. A continuous He-flow cryostat was used.

III. RESULTS AND DISCUSSION

A comparison of the zero-field-cooled (ZFC) and field-cooled (FC) magnetizations under 10 kOe is plotted in Fig. 1(a) showing a characteristic AFM peak at $T_N \sim 41$ K. As for magnetic susceptibility, $M(H)$ measurements (not shown) also discard the presence of any ferromagnetic component from a canted AFM state in the ordered magnetic phase. No signatures of disordered or paramagnetic moments are detected below T_N . Metamagnetic transitions were not observed up to 7 T in the $M(H)$ curves. $\text{Ba}_2\text{Co}_9\text{O}_{14}$ exhibits a high thermoelectric power of $180 \mu\text{V}/\text{K}$ at RT, reaching $\sim 236 \mu\text{V}/\text{K}$ around $T_S = 535$ K [13]. However, its high resistivity precludes it to be an effective thermoelectric material for energy conversion at high temperatures. Figure 1(b) shows the temperature dependence of the positive Seebeck coefficient (S) (p -type conductor) and the electrical resistivity measured between room temperature and 780 K. Below ~ 450 K the thermoelectric power $S(T)$ is nearly flat, as expected in a tunneling-assisted polaronic conductor. The rapid drop beyond T_S is compatible with a sudden increase in the density of p -type mobile carriers. The insulator-insulator transition takes place in the ~ 450 – 610 -K interval. The resistivity derivative [Fig. 1(b), inset] peaks at $T_{SS} \sim 567$ K which can be used to define the transition temperature [13].

All neutron powder-diffraction (NPD) patterns were successfully refined using the $R\text{-}3m$ crystal structure proposed by Sun *et al.* [10]. A detailed description of the structural parameters and agreement factors found at room temperature is given in Table I. Figure 2 displays a projection of the $\text{Ba}_2\text{Co}_9\text{O}_{14}$ structure with its five independent Co sites and octahedral and tetrahedral coordination polyhedra around cobalt atoms.

A. Magnetic symmetry and spin ordering at low temperature

Below $T_N \sim 41$ K the emergence of AFM order produces changes in the neutron-diffraction profile. Figure 3 compares the neutron-diffraction intensities recorded (on cooling) at 60 and 5 K. In agreement with Ref. [11], it is there shown that a set of new peaks of magnetic origin shows up below T_N . They prove the appearance of a new superstructure commensurate with the parent hexagonal cell, in such a way that the original parent cell gets doubled along the c axis. So, all new peaks associated to the magnetic superstructure can be successfully indexed considering the hexagonal pristine $R\text{-}3m$ cell and a magnetic propagation vector $\mathbf{k} = (003/2)$ (centered at the

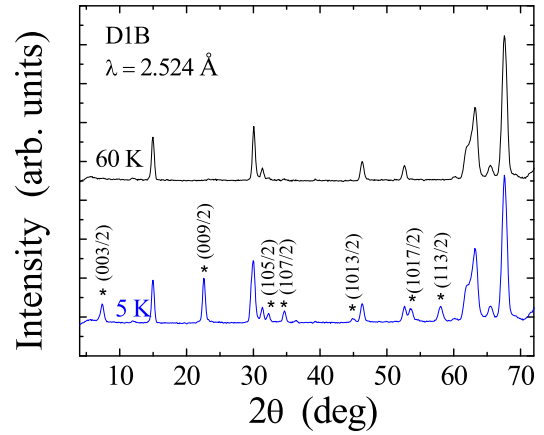


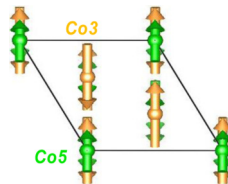
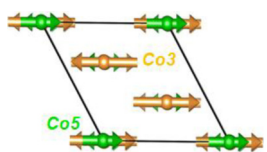
FIG. 3. Comparison of neutron-diffraction patterns (D1B) collected above (60 K) and below (5 K) $T_N \sim 41$ K. * labels the main magnetic reflections of the AFM phase as indexed in the parent (pristine) cell.

T point of the Brillouin zone). Some of the main magnetic reflections are shown in Fig. 3, where the indexation of the magnetic peaks refers to the parent $5.7 \text{ \AA} \times 5.7 \text{ \AA} \times 28.9 \text{ \AA}$ hexagonal cell.

Several magnetic (Shubnikov) space groups (MSGs) compatible with the $R\text{-}3m$ crystal symmetry and a $\mathbf{k} = (003/2)$ magnetic modulation were considered. Initially, two solutions were found to be fully compatible with our neutron-diffraction data. In both descriptions the only magnetic positions are those occupied by divalent cobalt atoms (Co3, Co5). So, the best fit is obtained using the C_c2/c (no. 15.90) and C_c2/m (no. 12.63) [see Table II, transformation to standard setting: $(1/3\mathbf{a} + 2/3\mathbf{b} - 4/3\mathbf{c}, -\mathbf{a}, 2\mathbf{c}; 0, 0, 0)$] MSGs which yield very similar goodness factors: [$R_B = 1.0(1.1), R_f = 1.2(1.3), R_{\text{Mag}} = 4.45(4.48), \chi^2 = 19.7(19.9)$ for $C_c2/c(C_c2/m)$].

Figure 4 displays the refined NPD pattern at 5 K using these magnetic groups yielding two possible magnetic models. They are both based on subgroups of the MSG $R\text{-}3m'$ but are not maximal subgroups. The primary magnetic irreducible representation (irrep) in both cases is mT_3^+ which produces the same spin configuration, but the direction of the spins is rotated by 90° between each other in the ab plane (due to a different orientation of the two-dimensional (2D) order parameter of mT_3^+). In the C_c2/c MSG Co3 and Co5 spins are constrained to $m = (m_x, 2m_x, m_z)$ but we experimentally observe that m_z is very small [$\leq 0.3(1)$] and difficult to distinguish from zero. In the second solution found (model 2, C_c2/m), the magnetic easy axis for the two magnetic cobalt positions follows the x direction of the hexagonal parent cell: $m = (m_x, 0, 0)$. A comparison of the two magnetic configurations is shown in Fig. 4. The additional 1D magnetic mode mT_2^+ compatible with the C_c2/c magnetic symmetry (model 1) allows the canting of Co3 and Co5 spins out of the a - b plane, and it is the responsible for the m_z magnetic component. The magnetic distortion mT_2^+ tilts the spins out of the a - b plane but keeps their alignment in Co3 and Co5 orbits, separately. According to our refinements, and within experimental errors, the amplitude of the mT_2^+ mode yields $m_z \approx 0.3(1)\mu_B/\text{Co}$. If, and only

TABLE II. Refined parameters for the C_c2/c and C_c2/m magnetic models compatible with NPD data at 5 K. The only Co ions providing a magnetic contribution are Co3 and Co5. The used setting is parentlike $(a, b, 2c; 0, 0, 0)$. The propagation vector is $\mathbf{k} = (0, 0, 3/2)$ [21].

Magnetic space group	Model 1 C_c2/c (no. 15.90)	Model 2 C_c2/m (no. 12.63)
Transformation to standard setting	$(1/3a + 2/3b - 4/3c, -a, 2c; 0, 0, 0)$ $a = b = 5.6928(4) \text{ \AA}, c = 57.7200(2) \text{ \AA}, \gamma = 120^\circ$	
Atomic Coordinates	Co3(0,0,0.1164(7) $m_x, 2m_x, m_z$) Co5 : (0,0,0 $m_x, 2m_x, m_z$)	Co3(0,0,0.1164(7) $m_x, 0, 0$) Co5 : (0,0,0 $m_x, 0, 0$)
Refined Moments (μ_B)	Co3 $(1.62(2), 3.24(2), 0.35(10))m_z \approx 0$ $m(\text{Co3}) = 2.83(3)\mu_B$ Co5 $(1.03(2), 2.06(4), -0.35(10))m_z \approx 0$ $m(\text{Co5}) = 1.82(4)\mu_B$	Co3 $(2.88(7), 0, 0)$ $m(\text{Co3}) = 2.88(7)\mu_B$ Co5 $(1.76(5), 0, 0)$ $m(\text{Co5}) = 1.76(5)\mu_B$
Magnetic irreps of $R\text{-}3m1'$ at the point T involving Co3 or Co5 spins	$mT_2^+(\alpha); mT_3^+(0, \beta)$	$mT_3^+(\alpha, 0)$
Magnetic structure		

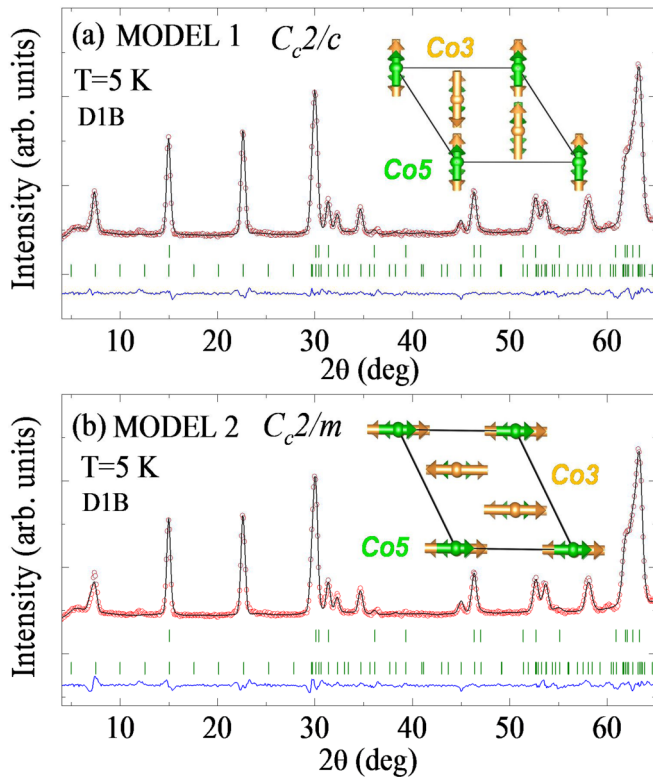


FIG. 4. Rietveld refinements of the neutron pattern registered at 5 K (D1B) using the magnetic space groups (a) C_c2/c (no. 15.90) with $m = (m_x, 2m_x, m_z)$ and (b) C_c2/m (no. 12.63) with $m = (m_x, 0, 0)$ in BNS description with $\mathbf{k} = (0, 0, 3/2)$.¹⁹ Additional details are given in Table II.

if we neglect this magnetic component both models become identical for the coupling between spins but rotated by 90° .

The magnetic moments refined at 5 K using C_c2/c and C_c2/m MSGs are given in Table II. In the C_c2/c symmetry the neutron refinements were done fixing $m_y = 2m_x$, which explains the reduced uncertainty for x, y coordinates shown in the table for this symmetry. The total size of the moments ($m = m_T$) at Co3 and Co5 sites is identical in both models: $m(\text{Co3}) = 2.8 \mu_B/\text{Co}$ and $m(\text{Co5}) = 1.8 \mu_B/\text{Co}$, the first one almost doubling the magnitude of the latter. This is in agreement with the analysis in Ref. [11] using representations and Bertaut's symmetry method.

After the considerations in the previous paragraphs, it becomes evident that any combination of the two described magnetic models will also be a solution that properly fits the experimental neutron pattern. In Figure 5 we show the common MSG $P_5\text{-}1$ (no. 2.7) that describes the more general magnetic solution for Co3 and Co5 sites compatible with the NPD pattern, as it incorporates the 2D irreps mT_3^+ of C_c2/c and C_c2/m permitting all possible directions for the associated order parameter: mT_3^+ along " (α, β) ." If we assume all spins parallel to the ab plane (namely, $\alpha = 0$ for mT_2^+) all the rotation angles in the plane between models 1 and 2 are experimentally feasible within $P_5\text{-}1$ [transformation to standard setting $(\mathbf{a}, -1/3\mathbf{a} + 1/3\mathbf{b} - 2/3\mathbf{c}, -2/3\mathbf{a} + 2/3\mathbf{b} + 2/3\mathbf{c}; 0, 0, 0)$].

Therefore, three clear conclusions emerge from the analysis of neutron data: (i) only divalent cobalt (Co3, Co5) positions are magnetic, spins getting ordered at T_N . This leads to a magnetic structure such as that represented in Fig. 6; (ii) single-crystal neutron studies are required to discern the easy axis of Co3 and Co5 atoms in $\text{Ba}_2\text{Co}_9\text{O}_{14}$ since neutron powder patterns below T_N are well reproduced using either

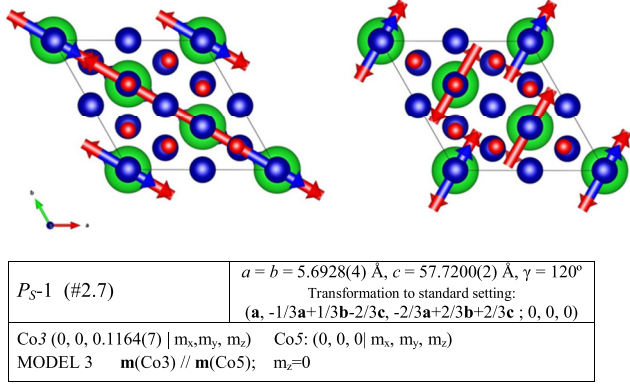


FIG. 5. Projection along the c axis of the magnetic structures with P_5-1 (no. 2.7) magnetic symmetry and the mT_3^+ (α, β) irrep activated along the directions $(0, \beta)$ (left) and $(\alpha, 0)$ (right). Both are compatible with NPD data at 5 K. Blue and red arrows represent spins at the Co3 and Co5 sites, respectively.

the C_c2/c and C_c2/m epikernels, or the P_5-1 kernel; (iii) below T_N the magnetic order is composed of AFM triple-layered blocks superposed along the hexagonal c axis. The magnetic unit cell ($a, b, 2c$) doubles the hexagonal parent cell along c and contains six triple-layered blocks, each one formed by an AFM sandwich of a central FM CdI₂-type layer (made of magnetic Co5 and nonmagnetic Co4 edge-sharing octahedra) antiferromagnetically coupled to the two outer

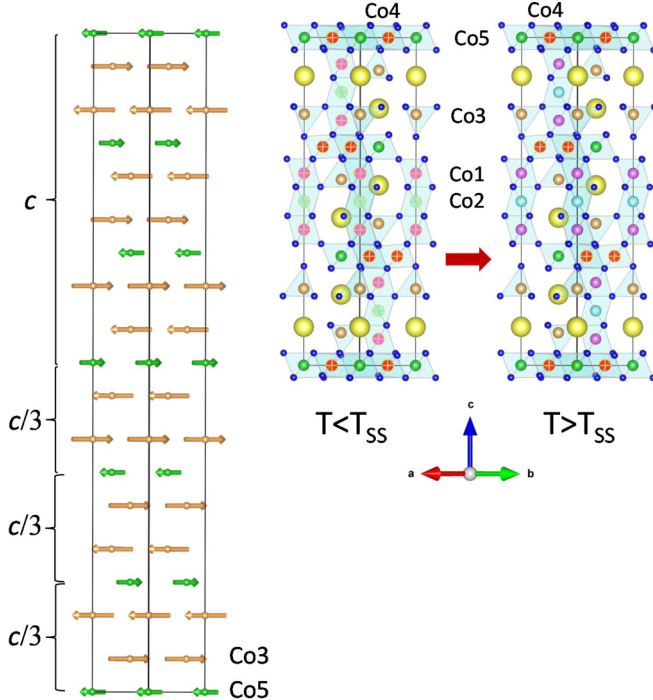


FIG. 6. Left: Schematic view of the AFM magnetic structure (only magnetic atoms in the ordered phase, Co3 and Co5, are shown). Right: Projection of the crystal structure illustrating the position of the cobalt sites changing its spin state across the transition (T_{SS}): Cobalt atoms in a low spin state have been labeled with the sign +. The figure illustrates which Co sites change their electronic configuration at the transition.

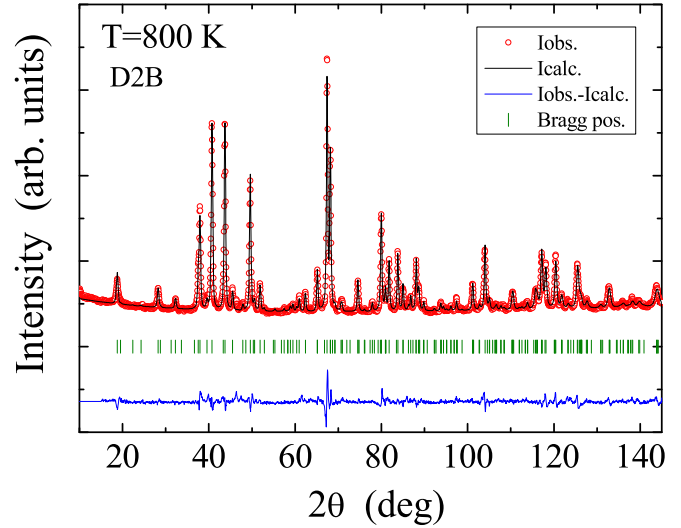


FIG. 7. Rietveld refinement (black line) of the NPD pattern for $\text{Ba}_2\text{Co}_9\text{CoO}_{14}$ at 800 K (D2B, red circles: experimental points; bottom blue line: difference).

layers both containing Co3 in a tetrahedral configuration. The intercoupling of successive triple blocks along c is also of AFM type (see Fig. 6), this being the origin of the $\mathbf{k} = (0, 0, 3/2)$ magnetic modulation given that there are three successive triple blocks in the chemical hexagonal cell.

Interestingly, at 5 K the size of the Co3 magnetic moments ($m_{\text{Co3}} = 2.8 \mu_B$) contrasts to that of antiparallel-coupled Co5 spins which add up to $m_{\text{Co5}} = 1.8 \mu_B$ regardless of the model (1, 2, or 3) considered. These numbers raise a question on the actual spin state and the real oxidation state of these divalent cobalt ions. Although it has been earlier assumed that Co3 and Co5 sites are Co^{2+} ions in a HS state, the different ordered magnetic moment they present could suggest a different electronic configuration and demands additional studies.

B. Study of the structural changes at the conductivity and spin-state transition

A neutron-diffraction study of the structural evolution across T_{SS} (the conductivity and spin-state transition) has been missing to date. Accurate Rietveld refinements can be obtained using the $R-3m$ structural model up to 800 K. The refined NPD pattern at 800 K is shown in Fig. 7. The structural parameters and atomic coordinates obtained from high-resolution NPD data obtained at 300, 420, 600, and 800 K are gathered in Table II.

The evolution of the hexagonal cell parameters and cell volume when increasing temperature is plotted in Figs. 8(a) and 8(b) (from SXRPD data) and reveals a rapid expansion around 567 K. Figure 8(c) moreover shows the linear thermal-expansion coefficient α_c deduced from $\alpha_c(T)$ as $\alpha_c = (1/c_0)(\Delta c/\Delta T)$ where the anomalous contribution to the lattice is particularly evident. The transition temperature T_{SS} perfectly matches that determined from transport measurements. The extra volume expansion across the transition is of about +0.7%. A deviation (on heating) of +1.05% and +2.1% from the conventional thermal lattice expansion is also observed in the individual a and c cell parameters, respectively.

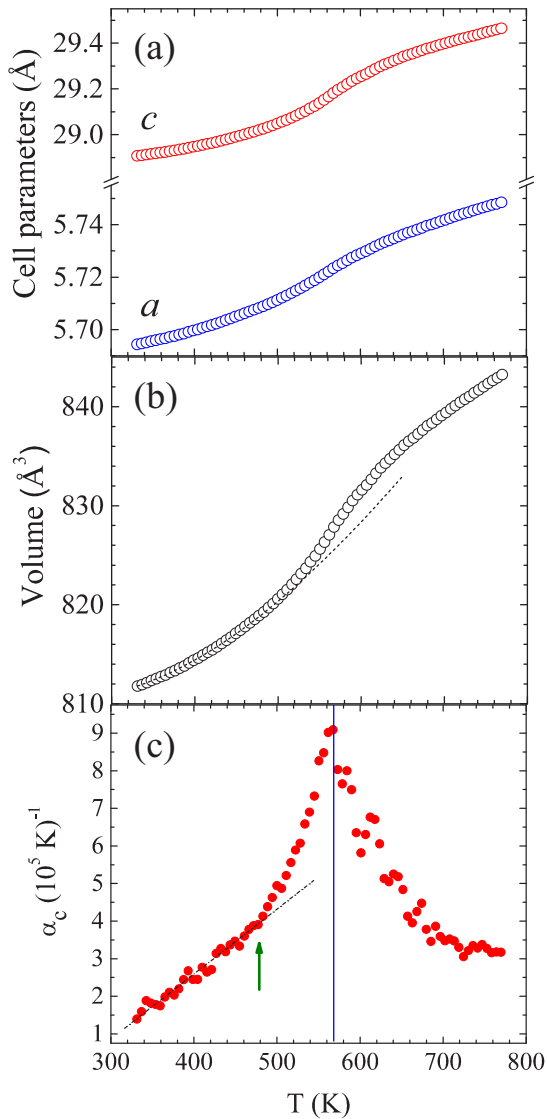


FIG. 8. SXRPD: Temperature dependence of (a) the a and c hexagonal cell parameters; (b) the unit-cell volume. The dotted black line is an eye guide that follows the expression $V_0 = V_1 + V_2\Theta \coth(\Theta/T)$ for $T < T_{SS}$; (c) the linear thermal-expansion coefficient α_c deduced from $c(T)$ as $\alpha_c = (1/c_0)(dc/dT)$. The blue line signals the transition temperature $T_{SS} = 567$ K.

As earlier confirmed in other cobaltites such as LaCoO_3 or $\text{GdBaCo}_2\text{O}_{5.50}$ [8,22], the changes in Co-O distances can be a direct fingerprint of spin-state transitions. To get further evidence of possible spin-state changes in the different Co sites in $\text{Ba}_2\text{Co}_9\text{O}_{14}$, the evolution of Co-O distances across T_{SS} for the octahedral ($\text{Co}_i, i = 1, 2, 3, 4$) and tetrahedral sites (Co_3) in the 300–800-K interval is plotted in Fig. 9, as obtained from NPD. Individual bond lengths and calculated bond valence sums (BVSs) [23] for Co ions are shown in Table III. We found marked discontinuities in the bond lengths on heating across the transition temperature: the thermal evolution at the two Co^{2+} sites (Co_3, Co_5) remains nearly flat below T_{SS} but it suddenly decreases at the transition very likely forced by an overall expansion of the $\text{Co}_3\text{-O}$ and $\text{Co}_5\text{-O}$ bonds. More precisely, (i) the average Co-O distances at Co_1 and Co_2

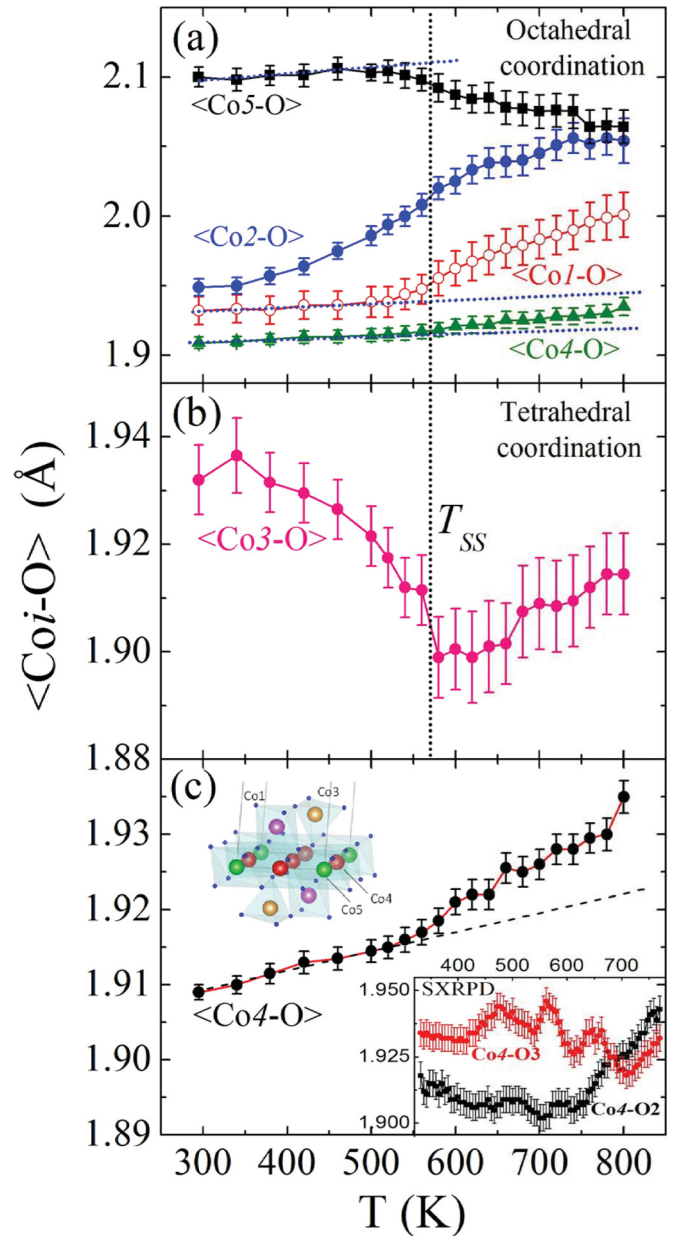


FIG. 9. Temperature evolution of the average $\text{Co}_i\text{-O}$ distances with (a) octahedral coordination CoO_6 ($\text{Co}_1, \text{Co}_2, \text{Co}_4, \text{Co}_5$), (b) tetrahedral coordination CoO_4 (Co_3) and (c) detailed evolution of the average $\text{Co}_4\text{-O}$ distance from NPD (the black dotted line marks $T_{SS} = 567$ K). Insets: distribution of Co_4 and Co_5 atoms within the CdI_2 -type layer, and evolution of individual $\text{Co}_4\text{-O}_2$ and $\text{Co}_4\text{-O}_3$ bond lengths obtained from SXRPD data.

octahedral sites clearly expand across the SS transition (+1.3% and +3.1%, respectively); (ii) the $\text{Co}_4\text{-O}$ bond length suffers a minor but nevertheless visible change ($\sim +0.4\%$) across the transition. The behavior shown here contrasts with the flat or negative slope reported by x rays [13]. In the octahedral trimer the expansion of Co_1 and Co_2 due to the SS transition compresses the $\text{Co}_3\text{-O}_4$ tetrahedra. Our neutron results reveal a significant $\text{Co}_3\text{-O}$ bonds contraction around T_{SS} (-1.7%), getting thermally expanded again in the high-temperature regime.

TABLE III. Nearest-neighbor Co i -O bond lengths, relative variation across T_{SS} from NPD data, and calculated bond-valence sum for Co ions.

	300 K	420 K	600 K	800 K	Relative variation 600–420 K
$d_{Co1-O1}(\text{Å}) \times 3$	1.968(4)	1.970(1)	1.974(7)	1.986(2)	+0.2%
$d_{Co1-O3}(\text{Å}) \times 3$	1.896(6)	1.902(9)	1.947(9)	2.012(8)	+2.4%
Calculated BVS	3.220	3.184	2.969	2.676	
$d_{Co2-O1}(\text{Å}) \times 6$	1.949(7)	1.964(7)	2.025(7)	2.054(6)	+3.1%
Calculated BVS	3.061	2.939	2.492	2.305	
$d_{Co3-O1}(\text{Å}) \times 3$	1.916(3)	1.911(9)	1.910(4)	1.887(5)	−0.05%
$d_{Co3-O2}(\text{Å})$	1.948(1)	1.948(1)	1.890(1)	1.939(2)	−2.9%
Calculated BVS	2.138	2.160	2.250	2.284	
$d_{Co4-O2}(\text{Å}) \times 2$	1.899(5)	1.903(3)	1.909(9)	1.903(4)	+0.3%
$d_{Co4-O3}(\text{Å}) \times 4$	1.918(3)	1.923(6)	1.933(5)	1.944(8)	+0.5%
Calculated BVS	3.387	3.344	3.267	3.232	
$d_{Co5-O3}(\text{Å}) \times 6$	2.100(5)	2.101(8)	2.086(4)	2.064(7)	−0.7%
Calculated BVS	1.997	1.986	2.068	2.195	

The CoO $_{6/3}$ layers (CdI $_2$ -type) are composed of ordered Co4 and Co5 octahedra in a 3:1 ratio forming a 2D network of triangles. Similarly to Co3 sites, the Co5 octahedra undergo a significant compression at the transition. On warming above T_{SS} , this Co $^{2+}$ site is the only one that exhibits a negative Co-O expansion coefficient. In this structure the Co $_3$ O $_{12}$ octahedral trimers are internally connected by corner-sharing CoO $_4$ tetrahedra (which also share corners with CdI $_2$ -type layers). Moreover it is also interesting to notice that the two extremes of each trimer share oxygens with respectively the inferior and superior CdI $_2$ -type layers running perpendicular to the trimer. In this way trimers act as vertical bridges connecting successive CoO $_{6/3}$ layers along c . The remarkable expansion observed in Co1O $_6$ and Co2O $_6$ octahedra is the signature of a thermally activated population of excited magnetic states—very likely HS—in these Co $^{3+}$ ions with consequences on the electron mobility along the trimers. At this point we must also emphasize the relevance for the electron mobility of the evolution found for the Co4-O bond length, as shown in detail in Fig. 9(c). The Co4O $_6$ octahedra in the CdI $_2$ -type layer are clearly more compacted than the rest. Nonetheless, as in the other two LS octahedra, a sudden expansion is evidenced at the transition indicative of an evolution toward a higher spin state at the Co4 site. The evolution of the individual Co4-O $_2$ and Co4-O $_3$ bond lengths shown in the inset of Fig. 9(c) from SXRPD data indicates that expansion of the Co4O $_6$ octahedra mainly occurs through elongation of the apical Co4-O $_2$ bond, whereas it can hardly overcome the compressive strain acting on O $_3$ (shared with the tetrahedron). Therefore, the origin of the conductivity drop can be twofold: the spin blockade along the octahedral trimers but also within the perpendicular CdI $_2$ -type layer.

Co2O $_6$ octahedra are flanked by Co1O $_6$ in the trimer. From the evolution of Co2-O in Fig. 9(a) one could be tempted to infer that the spin blockade along the octahedral trimers occurs first, due to a possible anomalous expansion of the Co2O $_6$ octahedra already from 350 K. However, the evolution of the linear thermal-expansion coefficient α_c in Fig. 8(c) sets the beginning of the anomalous expansion at ~ 475 K.

C. X-ray spectroscopic results

As concluded from the above neutron-diffraction results, a spin-state transition is expected at $T_{SS} \sim 567$ K at Co1 and Co2 trivalent ions lifting \mathcal{S} . At the same time, the Co-O distance decrease at divalent Co3 and Co5 sites could indicate SS changes in the opposite direction for these ions. We found Co1-O and Co2-O bond lengths between 1.93 and 1.95 Å at $T < T_{SS}$ which agrees with the expected theoretical values for Co $^{3+}$ ions in a LS configuration, [$d(\text{Co}^{3+}-\text{O})^{\text{VIII}}(\text{LS}) = 1.945$ Å and $d(\text{Co}^{3+}-\text{O})^{\text{VIII}}(\text{HS}) = 2.01$ Å)] [23]. On the other hand, at $T > T_{SS}$ bond lengths take values of 2.00–2.05 Å that better fit a Co $^{3+}$ HS model. The same method becomes less conclusive when applied to Co $^{2+}$ ions. The Co5-O bond lengths at $T < T_{SS}$ are rather compatible with a HS configuration (4T_1) than with a LS (2E) because theoretically $d(\text{Co}^{2+}-\text{O})^{\text{VIII}}(\text{HS})$ should be ~ 2.145 Å, while for the LS configuration we get 2.05 Å [23]. The observed Co5-O bond-length reduction on warming across T_{SS} could indicate a decrease in the average Co5 SS due to the appearance of LS ions or an increase in their proportion. This would be a natural consequence of the expected increase of the octahedral crystal-field energy [24,25]. Similar conclusions can be drawn on the electronic state of Co3-O with bond lengths decreasing across the transition. In this sense, the compression of local tetrahedra (octahedra) around Co3 (Co5) ions seems to partially compensate for the expansion of octahedra around the trivalent Co atoms. The electronic state of Co atoms varies accordingly to get adapted to these structural changes.

As observed when studying the magnetic structure by neutron diffraction, the only Co ions yielding a magnetic contribution to the structure are Co3 and Co5. Proposed models reveal that ordered m_{Co3} is larger than m_{Co5} . This suggests the Co3 site to be in a HS state while the Rietveld refinement could point to a different scenario for Co5. Assuming a similar weight of the orbital angular component to magnetization of Co $^{2+}$ ions at Co3 and Co5 sites the refined moment value obtained by neutron diffraction could be realized as due to a mixed LS/HS state at octahedral sites in an approximate 2:1 ratio.

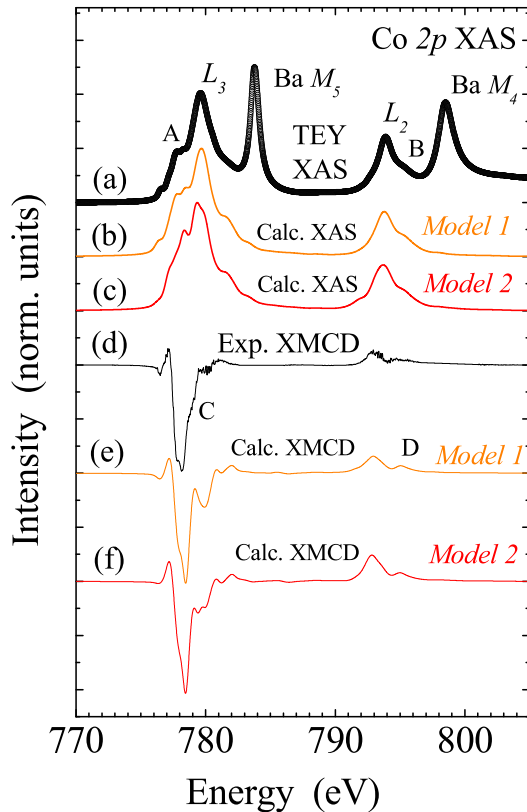


FIG. 10. (a) Experimental total-electron yield (TEY) measured Co $L_{2,3}$ XAS spectrum of $\text{Ba}_2\text{Co}_9\text{O}_{14}$ at 300 K (open black circles); (b) weighed sum of the calculated XAS spectra using Co^{2+} (O_h) in HS state (model 1); (c) weighed sum of the calculated XAS spectra using Co^{2+} (O_h) in a mixed LS:HS state (2:1 ratio) (model 2); (d) experimental Co $L_{2,3}$ XMCD signal of $\text{Ba}_2\text{Co}_9\text{O}_{14}$ at 300 K under an applied magnetic field of 6 T (black solid line); (e) weighed sum of the calculated XMCD signal using Co^{2+} (O_h) in HS state (model 1); (f) weighed sum of the calculated XMCD signal using Co^{2+} (O_h) in mixed LS:HS state (2:1 ratio) (model 2).

The experimental Co $L_{2,3}$ XAS spectrum of BCO at room temperature shown in Fig. 10 evidences a rich multiplet structure due to the presence of different Co sites with a differentiated electronic configuration and oxygen coordination thus complicating the identification of the several spectroscopic contributions. To ease this task we performed charge-transfer multiplet (CTM) calculations aimed at obtaining a characteristic XAS spectrum of Co ions at each structural site following their most likely electronic state [24,26–28] at room temperature, namely (i) LS state for the trivalent ions in CoO_6 octahedra (Co1, Co2, and Co4); (ii) HS state for the divalent ions in T_d local environment (Co3); and (iii) either a mixed LS:HS state (2:1 ratio) or a pure HS state for Co^{2+} with O_h symmetry (Co5). All calculations include a certain degree of covalency to O atoms. So, the theoretical Co $L_{2,3}$ XAS curve for BCO results from the addition of $6/9\text{Co}^{3+}O_h + 1/9\text{Co}^{2+}O_h + 2/9\text{Co}^{2+}T_d$ calculated spectra. We can see that the theoretical XAS spectrum turns out to be much more accurate when we do not consider any important contribution from a LS state at Co5 sites [Figs. 10(b) and 10(c)]. This is particularly noticeable by looking at the Co L_3 edge main spectral features. We here point out that the Ba

$M_{4,5}$ XAS (experimentally observed) contribution has not been included in the calculations. As pointed out above, the HS best calculation for Co5 sites comprehends a mixed ground state composed of $3d^7$ and $3d^8\bar{L}$ configurations (\bar{L} denotes a ligand hole at neighboring O atoms). Their corresponding weight has been found to be 0.88 and 0.12 which yields a total of 2.88 holes per Co5 ion. Other calculations with the charge-transfer excited configuration weighing up to $\sim 15\%$ of the total ground state can reasonably fit as well the experimental XAS. But, in any case these numbers are hard to reconcile with the idea of a charge transfer to ligands being the main mechanism causing the strikingly low value found for the ordered magnetic moment at these Co^{2+} sites. Furthermore, we also measured the x-ray magnetic circular dichroism (XMCD) spectra of BCO under a large applied magnetic field to crosscheck our hypothesis [Fig. 10(d)]. The paramagnetic response from BCO is large enough at 6 T so as to permit a detailed analysis and it turns out to be useful because here the large fraction of Co atoms occupying Co1, Co2, and Co4 sites do not nearly contribute at all in virtue of their $3d\bar{t}_{2g}^6$ electronic configuration (at least at low temperatures). This enhances the sensitivity of the spectra to the character of Co ions at divalent sites with respect to XAS. The calculated XMCD spectra for BCO for each of the two models considered reveal some differences, particularly at the Co L_2 edge where we can see that the eventual presence of $\text{Co}^{2+}O_h$ LS ions increases the amplitude of the main feature at ~ 795 eV [Figs. 10(e) and 10(f)]. This reflects a reduction in the orbital component of the magnetic moment [29,30]. The experimental XMCD spectrum seems to better agree with the HS model here too. Actually, the calculated spectra allow a quantitative analysis of the average orbital angular to spin moment ratio (m_L/m_S) per Co ion that yields 0.16 and 0.25 for the LS:HS (2:1) and pure HS models, respectively. For comparison, the experimental value we find for BCO at 100 K is 0.26(8) while this value increases up to 0.33(3) at 300 K. The calculated orbital component is definitely too low in the mixed spin model. The observed temperature evolution could be ascribed to the thermally assisted promotion of some Co ions into higher-lying states, particularly Co^{3+} as observed in similar cobaltites [31,32]. This will be further discussed when presenting x-ray emission spectroscopy (XES) results. Let us finally note that as expected, Ba ions are found not to contribute to the experimental XMCD differential signal.

Concerning the electronic configuration at Co3 and Co5 sites, large crystal-field energies are needed under O_h symmetry to favor a LS ground state in Co^{2+} , while these are usually not generated by oxygen ligands. For the tetrahedral coordination case the HS always appears as the most favorable state. In contrast, smaller-size Co^{3+} ions tend to be closer to the HS/LS crossover point and thus both configurations may exist [13]. So, we expect a lifted spin for both Co3 and Co5 divalent ions with a LS state component being less unlikely at the latter (octahedral) site. In contrast, Co1, Co2, and Co4 would mostly remain in a LS state at room temperature, getting excited into a HS state at $T > T_{SS}$ in agreement with the results shown in the preceding section.

To deepen the spectroscopic analysis of Co ions in $\text{Ba}_2\text{Co}_9\text{O}_{14}$ we also carried out Co $1s3p$ nonresonant (or $K\beta$ main) XES measurements. The $K\beta$ x-ray emission lines position and intensity respond to the effective number of

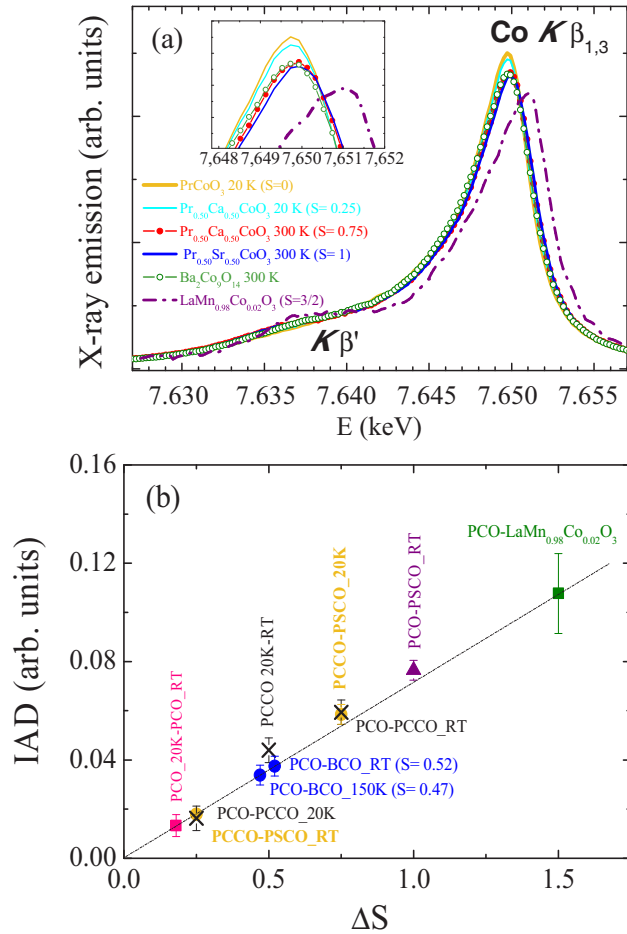


FIG. 11. (a) Co $K\beta$ emission curves of BCO at 300 K, PrCoO₃, Pr_{0.50}Ca_{0.50}CoO₃, Pr_{0.50}Sr_{0.50}CoO₃, and LaMn_{0.98}Co_{0.02}O₃ [34]. (b) IAD values diagram for the Co $K\beta$ emission spectra of BCO at 150 and 300 K as compared to those found for reference compounds (from Refs. [5,34,35]).

unpaired 3d electrons (i.e., to the net 3d shell spin). The $K\beta_{1,3}$ main emission line is a secondary process corresponding to the recombination of the 1s core hole that follows the photoabsorption process with a 3p electron. Meanwhile, the $K\beta'$ or satellite is a wider feature reflecting the exchange interaction of this secondary hole (in 3p orbitals) with the localized or itinerant electrons at the 3d band [24,26,33]. The comparative character of this technique called for the simultaneous acquisition of various reference compounds where the Co electronic state is better established; we have here selected PrCoO₃, Pr_{0.50}Ca_{0.50}CoO₃, Pr_{0.50}Sr_{0.50}CoO₃, and LaMn_{0.98}Co_{0.02}O₃. Figure 11(a) shows the experimental Co $K\beta$ lines of Ba₂Co₉O₁₄ at 300 K, PrCoO₃ (PCO) at 20 K ($S = 0$), Pr_{0.50}Ca_{0.50}CoO₃ (PCCO) at 20 and 300 K ($S = 0.25$ and $S = 0.75$, respectively) [5], Pr_{0.50}Sr_{0.50}CoO₃ (PSCO) at 300 K ($S = 1$) [34], and LaMn_{0.98}Co_{0.02}O₃ at 300 K ($S = 3/2$) [35]. We observe that the main differences as S decreases arise from the shift to lower energies of the $K\beta_{1,3}$ main line coupled to a decrease of the $K\beta'$ satellite. Qualitatively speaking, BCO seems to show an intermediate behavior between that of PCCO at low temperature and 300 K. More precisely, the average spin (S) of Co ions in BCO can be

derived from the sum of the individual expected spin values at each Co site. This nominally makes $S = 1/2$ for a Co²⁺ O_h HS model and $S = 0.43$ for the LS:HS (2:1) model (for Co5 sites too) earlier presented when analyzing XAS and XMCD results. The average spin value S for the HS model so far considered as the most plausible one from a spectroscopic point of view is unknown but it is reasonable to think of it being slightly lower than 0.50 following the reduction in the electron localization at Co 3d orbitals coming from the moderate charge transfer to the oxygen ligands previously commented. The integrated absolute difference (IAD) method allows the quantitative analysis of the emission lines [Fig. 11(b)]. This comparative method requires counting on the $K\beta$ emission spectrum of a (or various) reference(s) with a known electronic 3d configuration (i.e., oxidation and SS). The emission spectra of the compounds of interest can be compared by integrating the absolute difference between spectra (which corresponds to the IAD value) turning out that a direct relation (approximately linear, provided a similar local structure around the photoabsorbing ion in the compounds under study) relates the difference in the number of unpaired spins per photoabsorbing ion in the 3d shell (ΔS) with the IAD values, fulfilling that for $\Delta S = 0$ then IAD = 0 [36].

The IAD yields $S = 0.47(1)$ and $0.52(1)$ for BCO (S_{BCO}) at 100 and 300 K, respectively. These values nicely match the one resulting from considering Co ions at Co5 sites in a HS state in agreement with Co $L_{2,3}$ XAS and XMCD results. The evolution $\Delta S = 0.05$ observed between low temperature and 300 K can be ascribed to thermal activation ($k_B \Delta T \sim 12$ meV) of some electronic states [of (i) trivalent, (ii) divalent, or (iii) O_h divalent Co ions only]. This variation does not essentially affect our conclusions, although we can ascertain possible simple hypotheses to understand the deviations from the $S = 1/2$ expected value; while at 150 K the contribution of Co³⁺ ions to an excited SS must be minimal and nonzero covalency effects at Co5 sites may help to keep $S < 0.50$, at 300 K a small percentage of HS ions at trivalent sites ($S = 2$) may suffice to lift S_{BCO} up to 0.52, in line with earlier comments when discussing the temperature evolution of Co $L_{2,3}$ XMCD spectra.

IV. SUMMARY AND CONCLUSIONS

In this work we have presented a combined structural, magnetic, electric, and electronic characterization of the Ba₂Co₉O₁₄ oxide by means of neutron and x-ray diffraction, transport measurements, and x-ray-absorption and emission spectroscopies. Three possible magnetic space groups can account for the magnetic peaks and neutron intensities appeared below the Néel temperature ($T_N \sim 41$ K): C_c2/c , C_c2/m , and P_5-1 . All three are subgroups of the $R-3m1'$ grey group with a modulation centered at the T point of the BZ. The former MSG allows an out-of-plane AFM component which is experimentally found to be as small as to make it negligible. The real magnetic symmetry at low temperatures depends on the magnetic anisotropy in the ab plane, which cannot be unambiguously determined from neutron powder data. The Co spins order (in all three models) forming AFM triple-layered blocks where only Co3 and Co5 sites are magnetic; their

moments order antiparallel and present different magnitudes. We have unambiguously confirmed that ordered Co5 moments are far lower than expected for a Co^{2+} ion in a high spin ($S = 3/2$) configuration [$m(\text{Co5}) = 1.8\mu_{\text{B}}/\text{Co}$, to be compared to $m(\text{Co3}) = 2.8\mu_{\text{B}}/\text{Co}$].

Charge-transfer multiplet calculations point to a high spin configuration at all divalent Co sites, at the same time permitting us to rule out the presence of any significant amount of low spin Co5 ions. Our x-ray spectroscopic results also allow us to discard a reduced electronic localization at Co5 sites due to an unusually large charge transfer to O ligands. Independently, the analysis of measured Co $K\beta$ x-ray emission spectroscopy spectra agrees with this model. The strong moment reduction in Co5 is too large to be solely due to covalency effects and from present results we conclude that magnetic moments in Co5 atoms are not fully ordered. A partial magnetic disorder at this site is likely due to the concurrence of competing magnetic interactions. Thanks to the LS state of Co^{3+} sites, Co-O-O-Co supersuperexchange interactions are decisive for the magnetic order. On one hand SSE magnetic coupling through the Co5-O3-O2-Co3 path might compete with a Co5-O3-O3-Co5 SSE interaction. But, more likely, these supersuperexchange interactions could not overcome the magnetocrystalline anisotropy term—enhanced by the spin-orbit coupling—giving rise to a conflict between the easy directions of the two divalent sites. We attribute the small ordered moment found from Co5 (with octahedral environment) to the competition between the strong single-ion anisotropy of these divalent

ions and the weak supersuperexchange interactions with, respectively, its Co3 and Co5 nearest neighbors.

The $R-3m$ crystal symmetry remains stable up to 800 K. Diffraction results reveal a marked expansion across T_{SS} in the Co-O bond lengths around Co1 and Co2 octahedral sites. This anomalous expansion was also detected but it is weaker in the Co4O₆ octahedra. Concerning the divalent positions, the Co3-O bond contraction observed in the tetrahedron is larger than in the Co5O₆ octahedron. The origin of the conductivity drop on cooling is attributed to the mobile charge decrease at T_{SS} , generated both at the octahedral trimers and very likely also at the Co4O₆ octahedra within the CdI₂-type layer perpendicular to the trimers.

ACKNOWLEDGMENTS

We acknowledge financial support from the Spanish Ministry of Economy and Competitiveness (MINECO), through Projects No. MAT2015-68760-C2-2-P and No. MAT2012-38213-C02-02, and “Severo Ochoa” Programme for Centres of Excellence in R&D (SEV-2015-0496). The former are co-funded by ERDF of the European Union. We also acknowledge the ILL and the ALBA Synchrotron for granting beam time. C. Ritter and M. R. Wagner are acknowledged for technical assistance during neutron and Seebeck measurements, respectively. J.L.G.-M. and J.H.-M. are also grateful to J. M. Pérez-Mato and E. Pellegrin for fruitful discussions. J.P.-P. thanks CSIC for a JAE PREDOC contract.

-
- [1] S. Yamaguchi, Y. Okimoto, H. Taniguchi, and Y. Tokura, *Phys. Rev. B* **53**, R2926 (1996).
- [2] A. Podlesnyak, S. Streule, J. Mesot, M. Medarde, E. Pomjakushina, K. Conder, A. Tanaka, M.W. Haverkort, and D. I. Khomskii, *Phys. Rev. Lett.* **97**, 247208 (2006).
- [3] K. Asai, A. Yoneda, O. Yokokura, J. M. Tranquada, and G. Shirane, *J. Phys. Soc. Jpn.* **67**, 290 (1998).
- [4] S.Tsubouchi, T. Kyômen, M. Itoh, P. Ganguly, M. Oguni, Y. Shimojo, Y. Morii, and Y. Ishii, *Phys. Rev. B* **66**, 052418 (2002).
- [5] J. Herrero-Martín, J. L. García-Muñoz, K. Kvashnina, E. Gallo, G. Subías, J. A. Alonso, and A. J. Barón-González, *Phys. Rev. B* **86**, 125106 (2012).
- [6] K. Knizek, J. Hejtmánek, P. Novák, and Z. Jirák, *Phys. Rev. B* **81**, 155113 (2010).
- [7] J. L. García-Muñoz, C. Frontera, A. J. Barón-González, S. Valencia, J. Blasco, R. Feyherm, E. Dudzik, R. Abrudan, and F. Radu, *Phys. Rev. B* **84**, 045104 (2011).
- [8] C. Frontera, J. L. García-Muñoz, A. Llobet, and M. A. G. Aranda, *Phys. Rev. B* **65**, 180405(R) (2002); C. Frontera, J. L. García-Muñoz, A. E. Carrillo, M. A. G. Aranda, I. Margiolaki, and A. Caneiro, *ibid.* **74**, 054406 (2006).
- [9] A. Maignan, V. Caignaert, B. Raveau, D. Khomskii, and G. Sawatzky, *Phys. Rev. Lett.* **93**, 026401 (2004).
- [10] J. Sun, M. Yang, G. Li, T. Yang, F. Liao, Y. Wang, M. Xiong, and J. Lin, *Inorg. Chem.* **45**, 9151 (2006).
- [11] G. Ehora, S. Daviero-Minaud, M. Colmont, G. André, and O. Mentré, *Chem. Mater.* **19**, 2180 (2007).
- [12] Y. Li, M.W. Xu, and J. B. Goodenough, *J. Power Sources* **209**, 40 (2012).
- [13] J. G. Cheng, J. S. Zhou, Z. Hu, M. R. Suchomel, Y. Y. Chin, C. Y. Kuo, H. J. Lin, J. M. Chen, D. W. Pi, C. T. Chen, T. Takami, L. H. Tjeng, and J. B. Goodenough, *Phys. Rev. B* **85**, 094424 (2012).
- [14] F. Fauth, R. Boer, F. Gil-Ortiz, C. Popescu, O. Vallcorba, I. Peral, D. Fulla, J. Benach, and J. Juanhuix, *Eur. Phys. J. Plus* **130**, 160 (2015).
- [15] J. Rodríguez-Carvajal, *Physica B* **192**, 55 (1993); <http://www.ill.eu/sites/fullprof/>.
- [16] J. M. I. Aroyo, J. M. Perez-Mato, C. Capillas, E. Kroumova, S. Ivantchev, G. Madariaga, A. Kirov, and H. Wondratschek, *Z. Kristallogr.* **221**, 15 (2006); <http://www.crysl.ehu.es>.
- [17] M. I. Aroyo, A. Kirov, C. Capillas, J. M. Perez-Mato, and H. Wondratschek, *Acta Crystallogr. A* **62**, 115 (2006).
- [18] J. M. Perez-Mato, S. V. Gallego, E. S. Tasci, L. Elcoro, G. de la Flor, and M. I. Aroyo, *Annu. Rev. Mater. Res.* **45**, 217 (2015).
- [19] ISOTROPY Software Suite, iso.byu.edu, B. J. Campbell, H. T. Stokes, D. E. Tanner, and D. M. Hatch, *J. Appl. Crystallogr.* **39**, 607 (2006).
- [20] A. Barla, J. Nicolás, D. Cocco, S. M. Valvidares, J. Herrero-Martín, P. Gargiani, J. Moldes, C. Ruget, E. Pellegrin, and S. Ferrer, *J. Synchrotron Radiat.* **23**, 1507 (2016).
- [21] The magnetic space groups are referred to as the Belov-Neronova-Smirnova (BNS) notation. N. V. Belov, N. N.

- Neronova, and T. S. Smirnova, *Sov. Phys. Crystallogr.* **2**, 311 (1957).
- [22] P. G. Radaelli and S.-W. Cheong, *Phys. Rev. B* **66**, 094408 (2002).
- [23] R. D. Shannon, *Acta. Crystallogr. A* **32**, 751 (1976); I. D. Brown, *Z. Kristallogr.* **199**, 255 (1992).
- [24] F. De Groot and A. Kotani, *Core Level Spectroscopy of Solids* (Taylor and Francis, New York, 2008).
- [25] C. Piamonteze, P. Miedema, and F. M. F. de Groot, *Phys. Rev. B* **80**, 184410 (2009).
- [26] R. D. Cowan, *The Theory of Atomic Structure and Spectra* (University of California Press, Berkeley, 1981).
- [27] E. Stavitski and F. M. F. De Groot, *Micron* **41**, 687 (2010).
- [28] Parameters employed (eV) for Co1, Co2, Co4: Oh symmetry, $10D_q = 1.6$, $\Delta(C - T) = 3.0$, $U_{cd} - U_{dd} = 1.3$; for Co3: T_d symm., $10D_q = -0.3$, $\Delta = 7.0$, $U_{cd} - U_{dd} = 2.0$; for Co5: O_h symm., $10D_q = 0.8$, $\Delta = 5.0$, $U_{cd} - U_{dd} = 2.0$. Hopping T_{eg} and T_{t2g} energies were respectively fixed to 2.0 and 1.0 eV in all cases except for Co3 where we used $T_{eg} = 1.0$ eV, $T_{t2g} = 2.0$ eV. Slater integrals were kept at 80% (95%) of atomic values for Co^{3+} (Co^{2+}) ions calculations. Core and valence spin-orbit coupling was considered and kept at default values.
- [29] B. T. Thole, P. Carra, F. Sette, and G. van der Laan, *Phys. Rev. Lett.* **68**, 1943 (1992).
- [30] C. T. Chen, Y. U. Idzerda, H.-J. Lin, N. V. Smith, G. Meigs, E. Chaban, G. H. Ho, E. Pellegrin, and F. Sette, *Phys. Rev. Lett.* **75**, 152 (1995).
- [31] M. W. Haverkort, Z. Hu, J. C. Cezar, T. Burnus, H. Hartmann, M. Reuther, C. Zobel, T. Lorenz, A. Tanaka, N. B. Brookes, H. H. Hsieh, H.-J. Lin, C. T. Chen, and L. H. Tjeng, *Phys. Rev. Lett.* **97**, 176405 (2006).
- [32] N. Hollmann, M. W. Haverkort, M. Benomar, M. Cwik, M. Braden, and T. Lorenz, *Phys. Rev. B* **83**, 174435 (2011).
- [33] P. Glatzel and U. Bergmann, *Coord. Chem. Rev.* **249**, 65 (2005).
- [34] Unpublished data.
- [35] M. Sikora, K. Knizek, C. Kapusta, and P. Glatzel, *J. Appl. Phys.* **103**, 07C907 (2008).
- [36] G. Vankó, J.-P. Rueff, A. Mattila, Z. Németh, and A. Shukla, *Phys. Rev. B* **73**, 024424 (2006).